Journal of Solid State Chemistry ∎ (∎∎∎∎) ∎∎∎–∎∎∎

Contents lists available at ScienceDirect

Journal of Solid State Chemistry

journal homepage: www.elsevier.com/locate/jssc

Synthesis, crystal structure, and magnetism of $A_2Co_{12}As_7$ (A=Ca, Y, Ce–Yb)

Xiaoyan Tan [a], V. Ovidiu Garlea [b], Ping Chai [a], Andrey Y. Geondzhian [c], Alexander A. Yaroslavtsev [c,d], Yan Xin [e], Alexey P. Menushenkov [c], Roman V. Chernikov [f], Michael Shatruk [a,*]

[a] Department of Chemistry and Biochemistry, Florida State University, Tallahassee, FL 32306, USA
[b] Quantum Condensed Matter Division, Oak Ridge National Laboratory, Oak Ridge, TN 37831, USA
[c] National Research Nuclear University "Moscow Engineering Physics Institute", 115409 Moscow, Russia
[d] European XFEL GmbH, 22761 Hamburg, Germany
[e] National High Magnetic Field Laboratory, Tallahassee, FL 32310, USA
[f] DESY Photon Science, 22603 Hamburg, Germany

ARTICLE INFO

Article history:
Received 22 July 2015
Received in revised form
25 August 2015
Accepted 26 August 2015

Keywords:
Flux synthesis
Crystal growth
Arsenides
Itinerant magnetism
Mixed valence

ABSTRACT

Ternary intermetallics, $A_2Co_{12}As_7$ (A=Ca, Y, Ce–Yb), have been synthesized by annealing mixtures of elements in molten Bi at 1223 K. The materials obtained crystallize in the $P6_3/m$ variant of the $Zr_2Fe_{12}P_7$ structure type. The unit cell volume shows a monotonic decrease with the increasing atomic number of the rare-earth metal, with the exception of Ce-, Eu-, and Yb-containing compounds. An examination of these outliers with X-ray absorption near edge structures (XANES) spectroscopy revealed mixed valence of Ce, Eu, and Yb, with the average oxidation states of +3.20(1), +2.47(5), and +2.91(1), respectively, at room temperature. Magnetic behavior of $A_2Co_{12}As_7$ is generally characterized by ferromagnetic ordering of Co 3*d* moments at 100–140 K, followed by low-temperature ordering of rare-earth 4*f* moments. The 3*d*-4*f* magnetic coupling changes from antiferromagnetic for A=Pr–Sm to ferromagnetic for A=Ce and Eu–Yb. Polarized neutron scattering experiments were performed to support the postulated ferro- and ferrimagnetic ground states for $Ce_2Co_{12}As_7$ and $Nd_2Co_{12}As_7$, respectively.

1. Introduction

Intermetallics formed by rare-earth (R) and transition (T) metals represent a large family of compounds with many fascinating properties. Arguably, one of the most important applications of these materials is their use as the strongest permanent magnets, e.g., $Nd_2Fe_{14}B$ and $SmCo_5$ [1]. Other potential uses include magnetostrictive materials [2,3] and, more recently, magnetic refrigerants [4]. Despite the long-standing history of research on R–T intermetallics [5–7], a wealth of new structures and properties continues to be discovered every year. In this vein, an important innovative aspect is the exploration of less conventional synthetic methods that might allow access to new materials in the vast parameter space offered by the diverse elemental compositions and coordination numbers encountered in such structures [8].

Reactions in molten metal fluxes remain somewhat underused in the syntheses of R–T intermetallics, which are dominated by arc-melting and direct annealing techniques. Nevertheless, the use of various molten metals as reaction media has been steadily expanding, with the increased understanding that this method not only offers access to new materials, but also affords lower reaction temperatures and high-quality single crystals for physical property measurements [9].

Synthesis in Sn flux has been used as the method of choice for the preparation of materials in the ternary R–Co–P systems, affording crystal growth of ~100 compounds that crystallize in the PbFCl, $ThCr_2Si_2$, $HoCo_3P_2$, YCo_5P_3, $LaCo_8P_5$, $Zr_2Fe_{12}P_7$, and $Sc_5Co_{19}P_{12}$ structure types [10]. The availability of representative single crystals allowed detailed insight into magnetic properties and magnetically ordered structures for many of these materials, especially RCo_2P_2 [11–27]. In contrast, until recently there has been only scarce information on single-crystal growth in R–Co–As systems. RCo_2As_2 (R=La–Nd, Eu) [28], RCo_5As_3 (R=Y, Gd–Er) [29], and $RCo_{12}As_7$ (R=Y, Gd–Er) [30] have been reported, but only for $EuCo_2As_2$ was the structure established from the single-crystal X-ray diffraction experiment. Attempts to prepare these materials from Sn flux fail to produce phase-pure samples or representative single crystals. In 2012, Sefat and co-workers managed to obtain single crystals of $EuCo_2As_2$ by self-flux synthesis in CoAs melt and performed single-crystal measurements to establish, for the first

* Corresponding author.
E-mail address: shatruk@chem.fsu.edu (M. Shatruk).

http://dx.doi.org/10.1016/j.jssc.2015.08.038
0022-4596/

Table 1
Data collection and structure refinement parameters for $R_2Co_{12}As_7$.[a]

Compound	$Y_2Co_{12}As_7$	$Pr_2Co_{12}As_7$	$Nd_2Co_{12}As_7$	$Sm_2Co_{12}As_7$	$Eu_2Co_{12}As_7$	$Gd_2Co_{12}As_7$	$Tb_2Co_{12}As_7$	$Dy_2Co_{12}As_7$	$Er_2Co_{12}As_7$	$Yb_2Co_{12}As_7$
Temperature, K	293	293	293	293	293	293	293	293	293	293
λ, (Å)	0.71073	0.71073	0.71073	0.71073	0.71073	0.71073	0.71073	0.71073	0.71073	0.71073
Space group	$P6_3/m$	$P6_3/m$	$P6_3/m$	$P6_3/m$	$P6_3/m$	$P6_3/m$	$P6_3/m$	$P6_3/m$	$P6_3/m$	$P6_3/m$
Unit cell a, (Å)	9.3993(2)	9.4505(1)	9.443(4)	9.4230(1)	9.4509(1)	9.4173(4)	9.404(2)	9.3937(1)	9.3838(1)	9.3927(2)
c, (Å)	3.7368(1)	3.799(5)	3.790(8)	3.768(5)	3.775(5)	3.7588(2)	3.7435(9)	3.735(2)	3.719(4)	3.7138(1)
V, (Å^3)	285.90(1)	293.864(6)	292.7(3)	289.780(6)	292.024(6)	288.69(3)	286.70(5)	285.390(6)	283.628(6)	283.74(4)
Z	1	1	1	1	1	1	1	1	1	1
Crystal size, (mm^3)	$0.04 \times 0.02 \times 0.02$	$0.04 \times 0.01 \times 0.01$	$0.03 \times 0.01 \times 0.01$	$0.06 \times 0.05 \times 0.04$	$0.03 \times 0.02 \times 0.02$	$0.03 \times 0.03 \times 0.02$	$0.03 \times 0.01 \times 0.01$	$0.04 \times 0.02 \times 0.01$	$0.05 \times 0.02 \times 0.02$	$0.03 \times 0.02 \times 0.02$
ρ_{calc}, (g cm^{-3})	8.186	8.552	8.625	8.781	8.731	8.893	8.975	9.057	9.169	9.233
μ, (mm^{-1})	46.96	44.05	44.78	46.40	46.73	47.892	48.994	49.918	51.830	53.521
θ_{max}, (deg)	36.51	43.10	33.06	47.51	38.52	47.653	45.522	40.233	47.360	47.650
Reflections collected	4462	6176	2061	7058	4545	7063	6379	5329	6749	6331
R_{int}	0.024	0.021	0.042	0.020	0.023	0.025	0.046	0.031	0.028	0.034
Unique reflections	526	812	418	986	614	992	893	666	968	978
Parameters refined	30	30	30	30	30	30	30	30	30	30
R_1, wR_2 [$F_o > 4\sigma(F_o)$]	0.022, 0.049	0.018, 0.035	0.037, 0.078	0.017, 0.034	0.018, 0.035	0.021, 0.050	0.035, 0.068	0.029, 0.071	0.023, 0.051	0.028, 0.062
Diff. peak and hole, e (Å^{-3})	1.24, −1.30	1.29, −1.06	2.61, −2.71	1.52, −1.61	1.44, −1.95	1.81, −1.49	2.27, −2.73	3.27, −2.81	1.67, −2.11	2.51, −3.05
Goodness-of-fit	1.07	1.08	1.00	1.16	1.11	1.04	1.18	1.39	1.06	1.08

[a] Further details of the crystal structure determination may be obtained from Fachinformationszentrum Karlsruhe, D-76344 Eggenstein-Leopoldshafen, Germany, on quoting the depository numbers CSD 429922 through 429931.

time, magnetic properties of this material [31].

In an attempt to find alternative pathways to single crystals of R–Co arsenides, we have recently reported the use of molten Bi as an effective reaction medium for the crystal growth of RCo_2As_2 (R=La, Ce, Pr, Nd) [32,33]. Furthermore, this method afforded phase-pure bulk materials, thus allowing physical characterization to be carried out on both powder and single-crystal samples. In the present contribution, we describe a successful extension of reactions in Bi flux to the synthesis and crystal growth of $R_2Co_{12}As_7$ (R=Y, Ce–Yb), as well as $Ca_2Co_{12}As_7$. We also report investigation of the crystal structure and magnetic behavior of these materials by X-ray and neutron diffraction, transmission electron microscopy, and magnetic measurements.

2. Materials and methods

2.1. Synthesis

All manipulations during sample preparation were carried out in an argon-filled dry box (O_2 content <1 ppm). Powders of La (99.9%), Pr (99.9%), Y (99.6%), and As (99.99%), Ca dendritic pieces (99.98%), and Bi granules (99.997%) were obtained from Alfa Aesar and used as received. Eu metal chunks ($>99\%$) were acquired through the Materials Preparation Center at Ames Laboratory, which is supported by the US DOE Basic Energy Sciences. Ca and Eu metals were cut into small pieces. Ce and all other rare-earth metals were obtained by filing from metal chunks (Michigan Chemical Corporation, 99.9%) stored under oil, which was washed away with dry and air-free *n*-hexane before filing. Cobalt powder (Alfa Aesar, 99.5%) was additionally purified by heating in a flow of H_2 gas for 5 h at 775 K. For the synthesis of $A_2Co_{12}As_7$ (A=Ca, Y, Ce–Yb), starting materials were mixed in the A:Co:As:Bi=x:12:7:30 (x=2–3) ratio (total mass=5 g) and loaded into 10 mm inner diameter (i.d.) silica tubes, which were then sealed under vacuum ($<10^{-2}$ mbar). Carbonated silica tubes were used during the preparation of Ca-, Eu-, and Yb-containing samples. The mixtures were annealed at 1223 K for 8 days and cooled down naturally within the furnace. The Bi flux was removed by soaking the samples in a mixture of glacial acetic acid and 30% aqueous H_2O_2 (1:1 v/v) for 2–6 days, followed by successive washings with dilute HCl (1:1 v/v) and water. Hexagonal prism-shaped single crystals were selected from the reaction mixtures. The largest crystal was the one of $Ca_2Co_{12}As_7$ ($\sim 1 \times 0.2 \times 0.2$ mm^3); it was used for magnetic property measurement. The purity of bulk samples was checked by powder X-ray diffraction (PXRD).

2.2. Powder and single-crystal X-ray diffraction

Room temperature PXRD measurements were performed on a PANalytical X'Pert Pro diffractometer with an X'Celerator detector using Cu-$K\alpha$ radiation (λ=1.54187 Å). The patterns were recorded in the 2θ range from 10° to 80° with a step of 0.017° and the total collection time of 1 h. The PXRD data were processed with the HighScore Plus software package [34].

Single crystals of $A_2Co_{12}As_7$ were mounted on a goniometer head of a Bruker AXS SMART diffractometer equipped with an APEX-II CCD detector for room-temperature data collection. The data sets were recorded as ω-scans in steps of 0.3° and integrated with the Bruker SAINT software [35]. Crystal structures were solved and refined using the SHELX suite of programs [36]. All structures of $A_2Co_{12}As_7$ were solved in the $P6_3/m$ (No. 176) space group. A summary of pertinent information relating to unit cell parameters, data collection, and refinements is provided in Table 1.

2.3. Neutron scattering measurements

Neutron powder diffraction (NPD) experiments on $Nd_2Co_{12}As_7$ were carried out using the HB-2A high-resolution neutron powder diffractometer at the High Flux Isotope Reactor at Oak Ridge National Laboratory (ORNL). The $\lambda = 1.539$ Å monochromatic radiation was provided by a vertically focused Ge (115) monochromator. Measurements were performed on a sample of ~3 g held in a cylindrical vanadium container placed in a top-loading closed cycle refrigerator, covering a temperature range of 2–150 K. The data were collected by scanning the detector array consisting of 44 ^{3}He tubes in two segments, to cover the total 2θ range of 7–133° in steps of 0.05°. Overlapping detectors for a given step served to average the counting efficiency of each detector. More details about the HB-2A instrument and data collection strategies can be found in the original publication [37]. Rietveld refinements of the structures were carried out using the FULLPROF software [38].

NPD experiments performed at HB-2A were complemented by polarized neutron scattering measurements carried out using the hybrid spectrometer HYSPEC at the ORNL Spallation Neutron Source. The samples were prepared as compacted pellets, to avoid crystallite reorientation in applied magnetic field. The pelletized samples were loaded in Al cans and placed inside a 5 T vertical field cryomagnet, or a cylindrical assembly of permanent magnets that could be loaded in a closed cycle refrigerator to provide a vertical magnetic field of 0.1 T at the sample position. HYSPEC is a highly versatile direct geometry spectrometer that combines the time-of-flight (TOF) spectroscopy with the focusing Bragg optics [39]. The instrument was equipped with ^{3}He linear position sensitive tube detectors assembled into 20 sets of 8-packs that covered an angular range of 60° in the horizontal scattering plane and a vertical acceptance of 15°. The entire bank could be rotated about the sample, providing measurement at scattering angles of up to 135° depending upon the used incident energy (E_i). The polarized neutron beam was obtained by reflection from Heusler monochromator, and a Mezei flipper was used to flip the spin state of the incident neutron beam. For these polarized measurements we employed $E_i = 15$ meV ($\lambda = 2.335$ Å) that gave access to scattering angles of up to 105 °.

The scattering intensity for the polarized neutrons is given by the formula $I^{\pm} = |F_N|^2 \pm 2P_0 \cdot D \cdot F_N \cdot F_M + |F_M|^2$, where F_N and F_M are the nuclear and magnetic structure factors, P_0 is the incident neutron polarization, and D represents the depolarization factor that might occur in the sample. The nuclear-magnetic interference term of the scattering cross-section ($2P_0 \cdot D \cdot F_N \cdot F_M$) allows to enhance the magnetic sensitivity and remove the impact of the background on the peak-to-background ratio. With the incident polarization parallel to the applied field and sample magnetization, one can obtain the flipping difference spectra, $\mathrm{Diff} = I^+ - I^- = 4P_0 \cdot D \cdot F_N \cdot F_M$, in the case of crystal structures with inversion symmetry [40,41]. Note that the "flipping difference" technique only applies to samples that are ferro- or ferrimagnetically ordered under an applied magnetic field, where the incident polarization is parallel to the magnetization of the sample.

2.4. Magnetic measurements

Magnetic measurements were performed on polycrystalline samples and single crystals with a Quantum Design SQUID magnetometer MPMS-XL. DC magnetic susceptibility measurements were carried out in the temperature range of 1.8–300 K in an applied field of 1 mT. Isothermal field dependences of magnetization and hysteresis loops were measured with the magnetic field varying between −7 and 7 T.

2.5. X-ray absorption near-edge structure (XANES) spectroscopy

XANES spectra were measured at L_3-R absorption edges in the transmission mode. $Eu_2Co_{12}As_7$ and $Yb_2Co_{12}As_7$ spectra were measured in the range of 92–294 K at the beamline mySpot of BESSY-II storage ring (HZB, Berlin, Germany). $Ce_2Co_{12}As_7$ spectra were collected in the range of 80–200 K at beamline i811 of MAX IV Laboratory (Lund, Sweden). Nitrogen cryostat was used to cool down the samples during the measurements. The exact value of valence was extracted from the experimental spectra using the conventional fitting with the combination of Lorentzian, Gaussian, and arctangent curves.

2.6. Transmission electron microscopy (TEM)

TEM analysis was carried out on a probe aberration corrected sub-Å resolution JEOL JEM-ARM200cF microscope operated at accelerating voltage of 200 kV. The TEM data were obtained from thin electron-transparent pieces of a $Ca_2Co_{12}As_7$ single crystal. The sample was prepared by crushing the small single crystal with a mortar and pestle in methanol and dropping the suspension onto a carbon/formvar coated 200-mesh Cu TEM grid. Atomic resolution images along the major axis were obtained using scanning transmission electron microscopy high angle annular dark field imaging techniques (STEM-HAADF). STEM images were taken with the JEOL HAADF detector using the 7 c probe size, 30 μm CL aperture, 32 μs/pixel scan speed, and 8 cm camera length. The STEM resolution of the microscope was 0.78 Å. The inner detector collection angle was 76 mrad.

3. Results and discussion

3.1. Synthesis and crystal structure

The synthesis from Sn flux used for the preparation of $R_2Co_{12}P_7$ [42] failed to produce $R_2Co_{12}As_7$ (R=Y, Gd–Er). The latter were obtained by Stoyko and Oryshchyn by heating compacted pellets of constituent elements for 10 days at 970 K, then arc-melting the samples obtained, and finally re-annealing the ingots for 2 months at 970 K [30]. This method, however, did not afford good-quality single crystals. Moreover, the space group was assigned as $P\bar{6}$ based on PXRD data, but it will be shown below that the $R_2Co_{12}As_7$ structures are better described in the space group $P6_3/m$. To achieve the growth of single crystals and shorten the reaction time, we turned to the synthesis in Bi flux, a method that proved successful for preparation of a different family of ternary arsenides, RCo_2As_2. This method allowed the synthesis of $A_2Co_{12}As_7$ (A=Ca, Y, Ce–Yb) and the growth of representative single crystals that were easily selected from the final products. The syntheses were completed within 10–14 days and usually afforded single-phase materials (Figs. 1 and S1), except for the samples with R=Gd, Tm, and Yb, which contained Bi or CoAs as impurities. Numerous efforts failed to produce $La_2Co_{12}As_7$, similar to the non-existence of $La_2Co_{12}P_7$ in the $R_2Co_{12}P_7$ series [42].

Crystal structures of $R_2Co_{12}As_7$ grown from Bi flux were determined by single-crystal X-ray diffraction (Table 1). All compounds are isostructural and crystallize in the space group $P6_3/m$, in contrast to the earlier assignment of the space group as $P\bar{6}$ from PXRD data. The symmetry of the $R_2Co_{12}As_7$ lattices is thus different from that found for $R_2Co_{12}P_7$ ($P\bar{6}$) but consistent with the space group reported for $Ca_2Co_{12}As_7$ [43]. In general, the unit cell parameters and volume of $R_2Co_{12}As_7$ decrease as the atomic number of R increases (Figs. 2 and S2), as expected from the lanthanide contraction. Deviations to the smaller volume for R=Ce and to the larger volumes for R=Eu and Yb suggest the tendency

Please cite this article as: X. Tan, et al., J. Solid State Chem. (2015), http://dx.doi.org/10.1016/j.jssc.2015.08.038

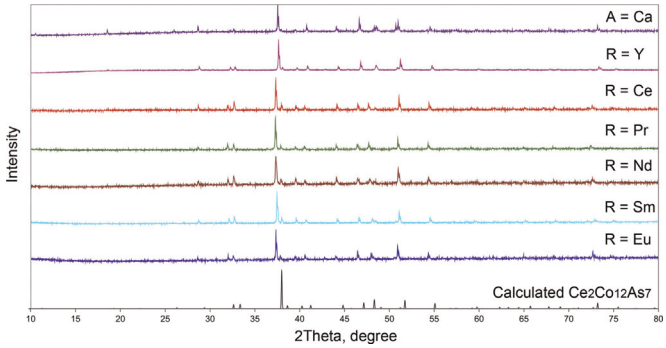

Fig. 1. Powder X-ray diffraction patterns of $A_2Co_{12}As_7$ (A=Ca, Y, Ce–Eu).

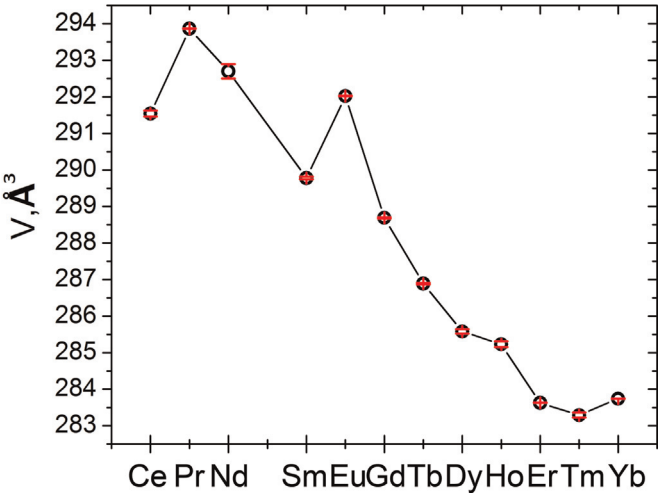

Fig. 2. Unit cell volumes of $R_2Co_{12}As_7$ (R=Ce–Yb). In general, the error bars are smaller than the symbol size.

of these metals toward higher (+4) and lower (+2) oxidation states, respectively.

Compounds $R_2Co_{12}As_7$ are isostructural to $Ca_2Co_{12}As_7$. A detailed analysis of the latter and its relation to the $Zr_2Fe_{12}P_7$ structure type was provided by Hellmann and Mewis [43] and Jeitschko et al. [44]. Briefly, the change in the space group from $P\bar{6}$ to $P6_3/m$ converts the unique As site (Wyckoff position 1*a* (0,0,0) in $P\bar{6}$) to the 2-fold As site (Wyckoff position 2*a* (0,0,1/4) in $P6_3/m$) with the (0,0,1/4) shift in the unit cell origin. In contrast to the $P\bar{6}$ structure, where adjacent 1*a* sites are separated by the whole unit cell period *c* in the [001] direction, in the $P6_3/m$ structure this separation is halved. Consequently, the space group change leads to half-occupancy of the 2*a* site due to the impossibly short separation between adjacent As2 positions along the *c* axis (*c*/2 ~ 1.8 Å). Such atomic arrangement becomes physically possible only if one consider the existence of domains, in which only one of the two half-occupied 2*a* positions along the *c* axis is filled in every unit cell. The existence of multiple domains with the As atoms occupying either all (0,0,1/4) or all (0,0,3/4) positions in a single domain results in the overall $P6_3/m$ symmetry. In addition, the disorder in the As positions, spaced at *c*/2 in the [001] direction, leads to the split of the nearby Co position 6*h* (*x*,*y*,1/4), which is situated either closer (~1.8 Å) to the vacant As2 site or further away (~2.3 Å) from the filled As2 site. It should be added that we found the use of the $P6_3/m$ space group to provide better refinement quality for all $A_2Co_{12}As_7$ structures. In contrast, refinements in the $P\bar{6}$ space group always led to substantially higher *R*-factors and the Flack parameter consistently converged to ~0.5, thus supporting the domain model described above.

The $Zr_2Fe_{12}P_7$ structure type, including its $P6_3/m$ variant, was described in detail before [43,44], and therefore, we will review only briefly the structure of $Nd_2Co_{12}As_7$ as an illustrative example (Table 2). The structure is built of Nd-centered As_6 trigonal prisms that share triangular faces along the *c* axis (Fig. 3a). The Nd–As distances are 2.984(1) Å. Wrapped around these prisms are chains of edge-sharing As_4 tetrahedra built entirely of As1 atoms and centered by Co1 atoms (Fig. 3b). The tetrahedra are slightly distorted, with Co–As distances varying from 2.378(2) Å to 2.392 (2) Å. Each tetrahedron shares an edge with an $NdAs_6$ prism, thus forming an extended framework with hexagonal channels (Fig. 3c). The nearest Co–Co distance between neighbor tetrahedra is 2.758(2) Å. In the center of hexagonal channels are chains of disordered As2 atoms, which are surrounded by a triangle of Co2 atoms at 2.270(3) Å each when the As2 position is filled, or by a triangle of Co3 atoms at 1.823(4) Å each when the As2 position is vacant. Due to additional coordination of three As1 atoms to each Co2 atom at 2.300(6) Å and 2.382(3) Å, there are Co2-centered As_4 tetrahedra that form triple-chains along the *c*-axis via vertex sharing (Fig. 3d). The complete polyhedral projection of the structure onto the *ab* plane is shown in Fig. 3e.

Table 2
Atomic parameters of the crystal structure of $Nd_2Co_{12}As_7$.

Atom	Wyckoff site	*x*	*y*	*z*	s.o.f.	U_{eq}
Nd1	2*c*	2/3	1/3	0.25	1	0.0071(2)
Co1	6*h*	0.0538(1)	0.4316(1)	0.25	1	0.0081(3)
Co2	6*h*	0.2770(4)	0.1538(6)	0.25	0.5	0.0081(7)
Co3	6*h*	0.2227(5)	0.1211(6)	0.25	0.5	0.0129(8)
As1	6*h*	0.29261(9)	0.40473(9)	0.25	1	0.0069(2)
As2	2*a*	0	0	0.25	0.5	0.0092(5)

To obtain further insight into the local atomic structure of these materials, TEM experiments were performed on thin single crystals of $Ca_2Co_{12}As_7$. Fig. 4a shows a STEM-HAADF image recorded along the [0001] (*c* axis) direction, with the schematic of the projected atomic structure as an inset. The white dots in these images are projected atomic columns, and their intensity depends on the number of atoms in the column and the atomic number (*Z*), i.e. the higher intensity indicates the presence of more atoms and/or a higher average *Z*. All the projected As and Co columns form a shape of a flower with the As2 column residing in the center. The crystallographic data show the interatomic distance along [0001] is 3.728 Å for all atoms, except for As2 atoms that show the As–As distance of 1.864 Å (*c*/2). A qualitative analysis of the image intensity, however, suggests that the intensity of the As2 column is similar to that of the As1 column, which agrees with the presence of As2 vacancies in the crystal structure. In addition, the Co2/Co3 columns, which appear as six nearest columns around the As2 column, exhibit lower intensity than the Co1 columns, which also implies the vacancies in the Co2/Co3 sites. Fig. 4b shows the atomic image along the $[10\bar{1}]/[2\bar{1}\bar{1}3]$ direction. The higher intensity columns are a mixture of As1 and Co1 atoms, which are at the distance of 4.51 Å along the projected direction (circled columns in the inset), whereas the lower intensity columns have interatomic distances of 10.14 Å. The As2 and Co2/Co3 columns with vacancies are seen as weak spots beside the higher intensity columns, although it is hard to distinguish the vacancy positions from this image.

To the best of our knowledge, this is the first reported TEM study of the $Zr_2Fe_{12}P_7$ family of structures. It reveals an interesting aspect of the vacancy-containing structure variant that crystallizes in the $P6_3/m$ space group. The vacancy ordering can be seen in the electron diffraction patterns (Fig. 4c, d) as streaks between the major diffraction spots. The separation between the vacancies is 16.32 Å in the $(01\bar{1}0)$ plane, which corresponds to doubling of the

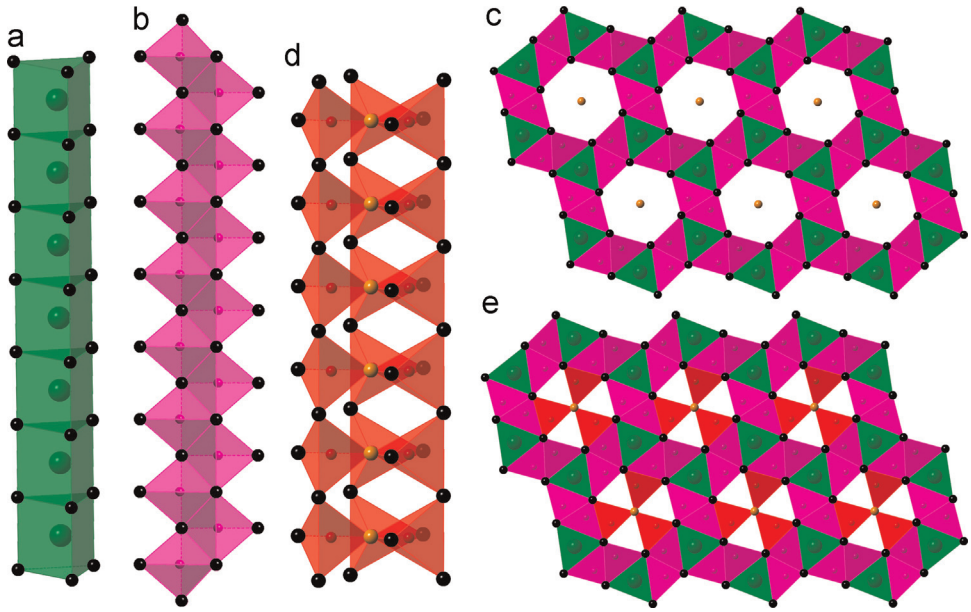

Fig. 3. Polyhedral representation of the crystal structure of $A_2Co_{12}As_7$ (A=Ca, Y, Ce–Eu): Columns of face-sharing $NdAs_6$ trigonal prisms (a) and edge-sharing $CoAs_4$ tetrahedra (b) share edges to from a framework with hexagonal channels that contain rows of disordered As2 atoms (c). The channels are additionally filled by Co2 atoms that surround the chains of As2 atoms and form triple-chains of vertex-sharing $CoAs_4$ tetrahedra due to coordination to the As1 atoms from the walls of the channels (d). The complete polyhedral build-up of the structure is shown in (e).

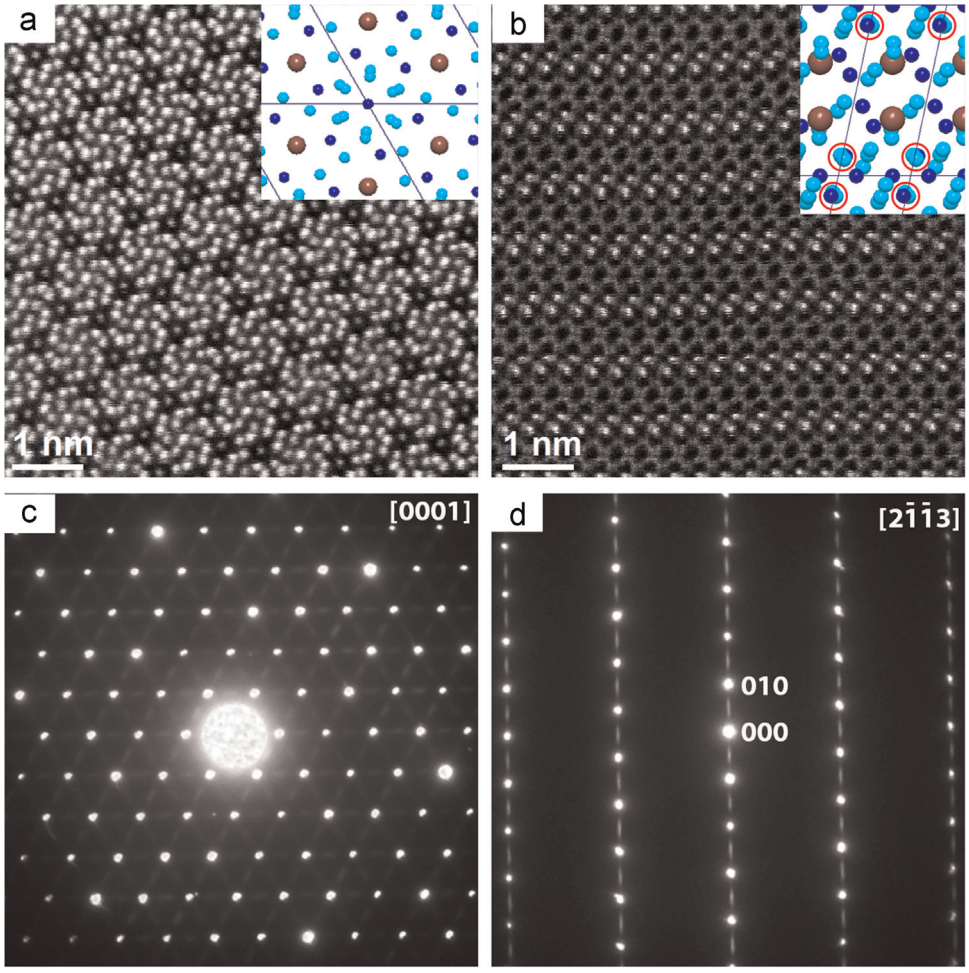

Fig. 4. STEM-HAADF atomic structure images taken along (a) [0001] and (b) [2$\bar{1}\bar{1}$3] directions and single-crystal electron diffraction patterns recorded along (c) [0001] and (d) [2$\bar{1}\bar{1}$3] directions. The insets depict projected atomic structures with Ca atoms in brown, As atoms in blue, and Co atoms in turquoise. (For interpretation of the references to color in this figure legend, the reader is referred to the web version of this article.)

Please cite this article as: X. Tan, et al., J. Solid State Chem. (2015), http://dx.doi.org/10.1016/j.jssc.2015.08.038

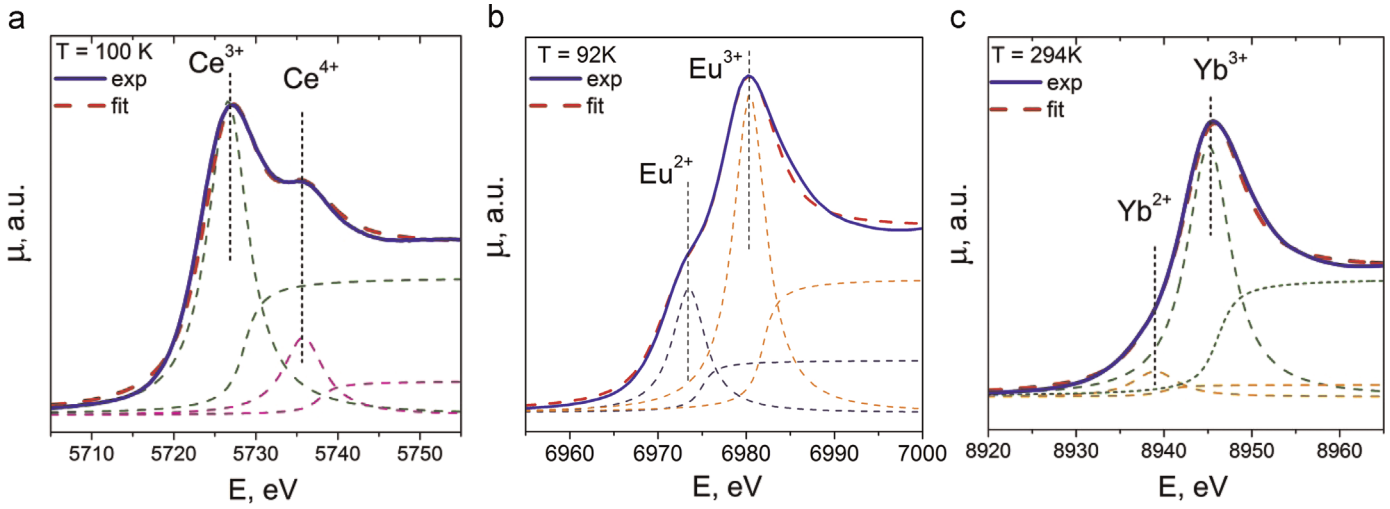

Fig. 5. L_3-R XANES spectra of $R_2Co_{12}As_7$ with R=Ce (a), Eu (b), and Yb (c) at 100 K, 92 K, and 294 K, respectively.

a or *b* axis. Based on this finding, it would be interesting to explore the character of vacancy distribution in other $R_2Co_{12}As_7$ structures by TEM.

3.2. XANES spectroscopy

Based on the trend in unit cell volumes in the $R_2Co_{12}As_7$ series (Fig. 2), the valence of Ce, Eu, and Yb should deviate from +3. Therefore, these samples were studied by XANES spectroscopy at the L_3 edge of the corresponding R metal. As shown in Fig. 5, the spectra of all three compounds contain two components that correspond to Ce^{3+}/Ce^{4+}, Eu^{2+}/Eu^{3+}, and Yb^{2+}/Yb^{3+} ions. In each case, the component contributing to the +3 oxidation state dominates the spectrum. Fitting the spectra of $Ce_2Co_{12}As_7$ resulted in the average Ce oxidation state of +3.20(1) in the range from 80 to 300 K (Fig. S3). The average oxidation state of Eu increased as the temperature was lowered, from +2.47(5) at 294 K to +2.73 (1) at 92 K (Fig. S4), in accord with the higher chemical pressure exerted on the Eu crystallographic site by the lattice contraction at lower temperature [23]. Only slight mixed-valence was established for $Yb_2Co_{12}As_7$, with the average Yb oxidation state of +2.91(1) in the range from 150 to 294 K (Fig. S5).

The XANES results conclusively confirmed the mixed valence of rare-earth metals in $R_2Co_{12}As_7$ with R=Ce, Eu, Yb. Only in the Eu-containing compound, however, does the average oxidation state exhibit the strong temperature dependence and the large deviation from the integer value. The behavior of these materials is distinctly different from that of their $R_2Co_{12}P_7$ analogs, among which only $Ce_2Co_{12}P_7$ deviates from the uniform decrease in the unit cell volume as the atomic number of R increases [13], while $Eu_2Co_{12}P_7$ and $Yb_2Co_{12}P_7$ follow the general trend, which suggests they exist in the +3 oxidation state. These observations correlate with the lower electronegativity of As relative to P, since Ce, Eu, and Yb clearly exhibit the tendency to lower oxidation states in $R_2Co_{12}As_7$ as compared to those in $R_2Co_{12}P_7$.

3.3. Magnetic properties

$A_2Co_{12}As_7$(A=Ca, Y, Yb). The magnetic properties of all studied $A_2Co_{12}As_7$ materials are summarized in Table 3. Since $Ca_2Co_{12}As_7$ and $Y_2Co_{12}As_7$ contain diamagnetic ions in the A site, they serve as model compounds for evaluating the magnetic behavior of Co sublattice. Both of them exhibit ferromagnetic (FM) ordering of Co moments at 38 K and 115 K, respectively (Fig. 6a, b). The

Table 3
Magnetic properties of $A_2Co_{12}As_7$ (A=Ca, Y, Ce–Yb).

Compound	T_C (Co), K	T^* (R),[a] K	M_{max} (100 K), μ_B/f.u.	M_{max} (1.8 K), μ_B/f.u.	M_{calc} (R^{3+}), μ_B	Co(3*d*)–R (4*f*) coupling
$Ca_2Co_{12}As_7$	38	–	–	1.83	–	–
$Y_2Co_{12}As_7$	115	–	2.07	3.78	–	–
$Ce_2Co_{12}As_7$	90	27	–	2.16	2.14	FM
$Pr_2Co_{12}As_7$	107	20	2.71	6.44	3.20	AFM
$Nd_2Co_{12}As_7$	113	50	2.73	4.40	3.28	AFM
$Sm_2Co_{12}As_7$	110	25	2.66	3.21	0.72	AFM
$Eu_2Co_{12}As_7$	136	136	4.95	6.49	0	FM
$Gd_2Co_{12}As_7$	117	117	5.67	22.6	7	FM
$Tb_2Co_{12}As_7$	131	84	7.73	18.5	9	FM
$Dy_2Co_{12}As_7$	128	69	6.52	18.2	10	FM
$Ho_2Co_{12}As_7$	139	45	8.25	21.6	10	FM
$Er_2Co_{12}As_7$	116	46	6.37	19.1	9	FM
$Tm_2Co_{12}As_7$	136	31	5.90	14.6	7	FM
$Yb_2Co_{12}As_7$	60	–	–	2.39	4	–

[a] T^* was estimated as the point at which the magnetic susceptibility showed an abrupt increase or decrease in the regime below the ordering temperature (T_C) of the Co sublattice.

divergence of the zero-field-cooled (ZFC) and field-cooled (FC) magnetic susceptibility curves obtained under applied field of 1 mT indicates some magnetic anisotropy in the Co sublattice. The anisotropy was further confirmed by magnetic measurements on an oriented single crystal of $Ca_2Co_{12}As_7$ which revealed the strong preference of Co moments to orient along the hexagonal *c* axis (Fig. S6). For $Ca_2Co_{12}As_7$, the field-dependent magnetization measured at 1.8 K reached the maximum of 1.83 μ_B per formula unit (f.u.) at 7 T, but did not saturate (Fig. 6a, inset), while for $Y_2Co_{12}As_7$, the M_{sat} value of 3.78 μ_B per f.u. was reached under the same conditions (Fig. 6b, inset). Thus, one can expect that (1) the Co sublattice in $A_2Co_{12}As_7$ will tend to exhibit FM ordering and (2) the values of T_C and M_{sat} might show significant dependence on the ionic size and charge of the electropositive metal, A, which impact the separation between the Co atoms and the filling of the Co 3*d* band, respectively.

Similar to the Ca- and Y-containing compounds, $Yb_2Co_{12}As_7$ exhibits FM ordering at T_C=60 K (Fig. 6c). This phase transition is also attributed to the ordering of Co magnetic moments. The mixed-valent +2.91 oxidation state established by XANES spectroscopy is dominated by the typically magnetic Yb^{3+} ion. Therefore, one could expect that the Yb sublattice should also contribute to the magnetic behavior of $Yb_2Co_{12}As_7$. Nevertheless,

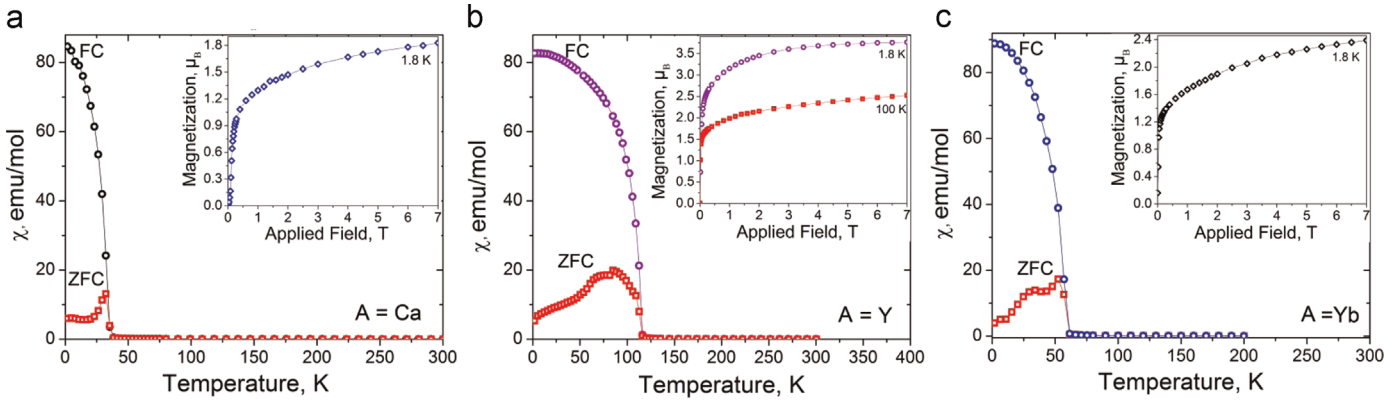

Fig. 6. Temperature dependence of zero-field-cooled (ZFC) and field-cooled (FC) magnetization at 1 mT and isothermal field dependence of magnetization (inset) for $Ca_2Co_{12}As_7$ (a), $Y_2Co_{12}As_7$ (b), and $Yb_2Co_{12}As_7$ (c).

by comparing the magnetic susceptibility curves of Ca-, Y-, and Yb-containing samples, no clear contribution from the Yb magnetic moments can be discerned. In fact, the ZFC and FC susceptibility and field-dependent magnetization curves for $Yb_2Co_{12}As_7$ are very similar to those found for $Ca_2Co_{12}As_7$, suggesting the FM ordering of Co moments at 60 K and negligible participation of Yb moments in the magnetic behavior.

It is interesting to compare the magnetic behavior of $Yb_2Co_{12}As_7$ and $YbCo_{12}P_7$. The FM ordering temperature of $Yb_2Co_{12}As_7$ (60 K) is much closer to the T_C of $Ca_2Co_{12}As_7$ (38 K) than to the T_C of $Y_2Co_{12}As_7$ (115 K). In contrast, $YbCo_{12}P_7$ shows T_C similar to the values observed for $R_2Co_{12}P_7$ materials with R^{3+} ions. Such behavior of $YbCo_{12}P_7$ is in line with its following the general trend for the R-dependent unit cell volume observed in the $R_2Co_{12}P_7$ series, which suggests the oxidation state of Yb^{3+}. It is intriguing that even the small deviation from this oxidation state in $Yb_2Co_{12}As_7$ has such pronounced influence on the FM phase transition temperature. In this context, it would be interesting to compare the magnetic behavior of $YbCo_{12}P_7$ to that of $Ca_2Co_{12}P_7$ and $Y_2Co_{12}P_7$, but unfortunately, the latter compounds were reported relatively recently [43,45], and their magnetic properties are unknown.

$R_2Co_{12}As_7$ (R=Ce, Pr, Nd, Sm, Eu, Gd). The temperature dependences of magnetic susceptibility, measured on polycrystalline samples of $R_2Co_{12}As_7$ (R=Ce, Pr, Nd, Sm, Eu, Gd), indicate the FM ordering of Co moments with T_C = 90, 107, 113, 110, 136, and 117 K, respectively (Fig. 7a, 7d, and S7). These values are similar to the ordering temperature of $Y_2Co_{12}As_7$ (115 K), although the T_C appears to increase as the lanthanide ionic radius decreases. A

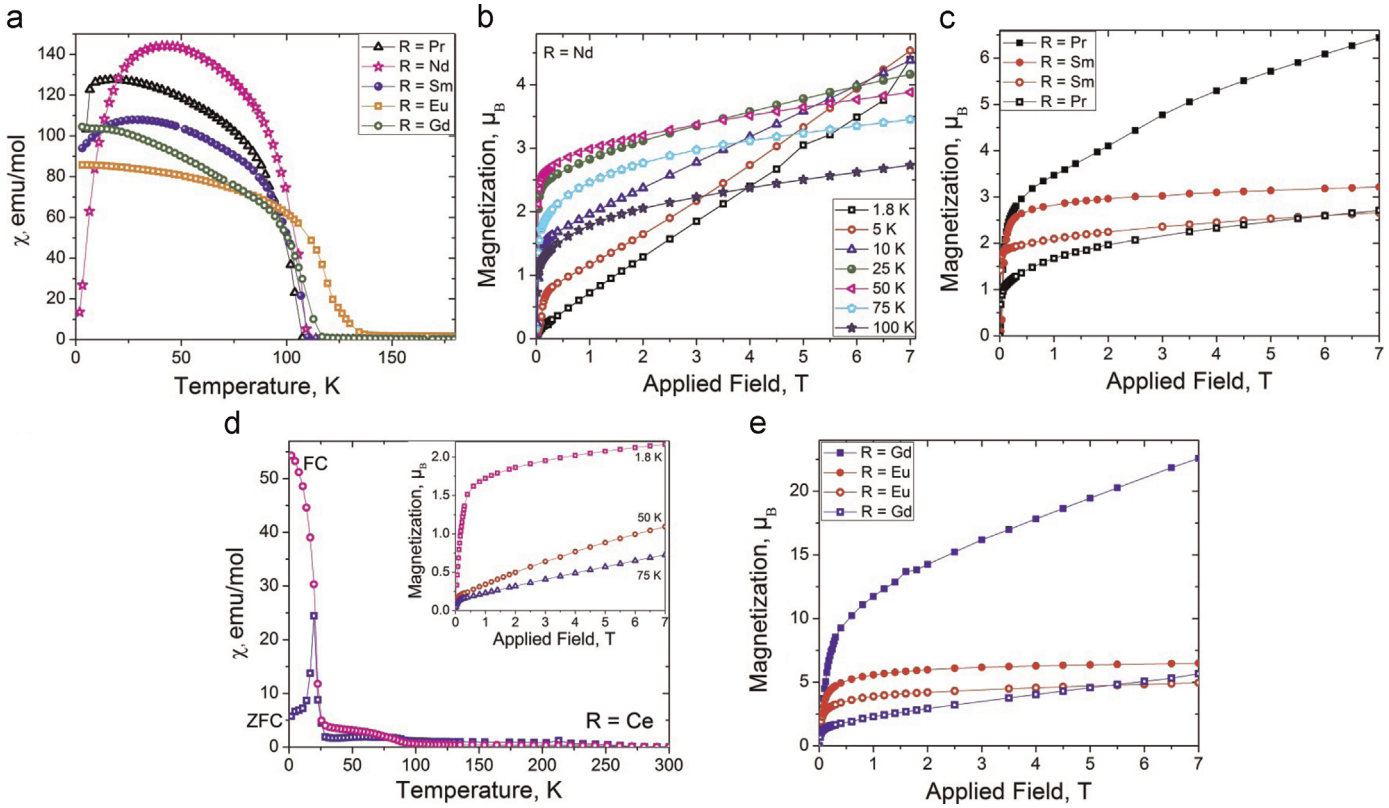

Fig. 7. (a) Temperature dependence of field-cooled magnetization for $R_2Co_{12}As_7$ (R=Pr–Gd) at 1 mT. (b) Isothermal field dependences of magnetization for $Nd_2Co_{12}As_7$ at various temperatures. (c) Isothermal field dependences of magnetization for $Pr_2Co_{12}As_7$ and $Sm_2Co_{12}As_7$ at 100 K (empty symbols) and 1.8 K (filled symbols). (d) Temperature dependence of field-cooled and zero-field-cooled magnetization for $Ce_2Co_{12}As_7$ at 1 mT. Inset: isothermal field dependences of magnetization at various temperatures. (e) Isothermal field dependences of magnetization for $Eu_2Co_{12}As_7$ and $Gd_2Co_{12}As_7$ at 100 K (empty symbols) and 1.8 K (filled symbols).

deviation from this general trend is only seen for $Eu_2Co_{12}As_7$, which could be explained by modification of the electronic structure of this material due to the mixed valence of Eu that might promote stronger magnetic exchange. Similar magnetic behavior in the Co sublattice was also observed for $R_2Co_{12}P_7$, with the Co FM ordering temperature varying in the range of 142–158 K [13].

The magnetic susceptibility for R=Pr, Nd, and Sm reaches the maximum value at 20, 50, and 25 K, respectively, and then decreases as the temperature is lowered. Such behavior is characteristic of AFM coupling between the R 4*f* and Co 3*d* magnetic moments, suggesting the ferrimagnetic (FiM) ground state for these materials. This finding is also in accord with the FiM behavior reported for $Pr_2Co_{12}P_7$ and $Nd_2Co_{12}P_7$ [13], as well as for $PrCo_2As_2$ and $NdCo_2As_2$ [33]. The AFM 4*f*-3*d* coupling is well illustrated by the magnetization isotherms recorded for $Nd_2Co_{12}As_7$ at different temperatures (Fig. 7b). The isotherms obtained at 100 and 50 K exhibit fast initial increase in low fields due to the FM ordering of Co moments. The higher rise observed at 50 K is explained by the growth of Co FM domains as the temperature is lowered. The isotherms obtained below 50 K, however, exhibit gradual suppression of the low-field magnetization, and the curve obtained at 1.8 K is essentially linear. Such behavior can be explained by the gradual ordering of Nd 4*f* moments in the direction antiparallel to the magnetization of the Co 3*d* moments. It should be emphasized that the M_{max} value observed at 100 K ($\sim$2.7 μ_B) is similar for all three materials (Fig. 7b and c) and slightly larger than the value obtained for $Y_2Co_{12}As_7$ at the same temperature (Fig. 6b, inset). This observation is also in agreement with the initial ordering of Co 3*d* moments around 110 K, followed by the ordering of R 4*f* moments at lower temperatures.

The behavior of $Ce_2Co_{12}As_7$ in the low temperature range is quite different. While the increase in magnetic susceptibility at 90 K can be attributed to the FM ordering of Co moments, the susceptibility shows a much more abrupt increase at 27 K (Fig. 7d). This second magnetic transition can be ascribed to FM ordering of Ce moments, given that the Ce oxidation state is close to +3. The isothermal magnetization measured at 75 and 50 K exhibits the initial fast growth due to the ordered Co moments (Fig. 7d, inset), but the observed moment is much lower than in the case of $R_2Co_{12}As_7$ with R=Y, Pr, Nd, or Sm. At higher fields, a linear increase is observed due to the response of paramagnetic Ce sublattice. The M_{max} values per f.u. are 0.72 and 1.09 μ_B at 75 and 50 K, respectively. At 1.8 K, the magnetization is characteristic of a ferromagnet, but M_{sat} remains relatively low, only 2.16 μ_B at 7 T. We will return to the discussion of magnetic ordering in this compound in the neutron scattering section.

In the case of $Eu_2Co_{12}As_7$ and $Gd_2Co_{12}As_7$, the magnetism of the $4f^7$ Eu^{2+} and Gd^{3+} ions is only due to the spin component of the total angular momentum. (Despite the mixed valence of Eu, the contribution from the Eu^{3+} ion with a non-magnetic $J=0$ ground state can be neglected.) Therefore, the effect of the magnetocrystalline anisotropy of rare-earth ion on the magnetic properties should be small. Neither of these compounds exhibits a discernable up or down turn in the FC magnetic susceptibility curve at lower temperatures (Fig. 7a). This observation suggests that the ordering of both 3*d* and 4*f* moments sets in simultaneously, at 117 K for $Gd_2Co_{12}As_7$ and 136 K for $Eu_2Co_{12}As_7$. The isothermal magnetization curves measured for $Gd_2Co_{12}As_7$ (Fig. 7e) clearly show a large difference between 100 K (M_{max} =5.67 μ_B per f.u.) and 1.8 K (M_{max}=22.6 μ_B per f.u.). Taking into account the theoretically expected contribution of 14.0 μ_B from two Gd^{3+} ions, we can conclude FM coupling between Gd and Co moments.

The situation is more complicated in the case of $Eu_2Co_{12}As_7$, because Eu exhibits mixed valence with strong temperature dependence (see Section 3.2). Given the isoelectronic nature of Eu^{2+} and Gd^{3+}, we could assume that the 3*d*-4*f* coupling in $Eu_2Co_{12}As_7$ is also FM. Indeed, the isothermal magnetization curves collected at 100 and 1.8 K exhibit typical FM behavior (Fig. 7e). Nevertheless, the M_{max} at 100 K is similar (4.95 μ_B) but the M_{max} at 1.8 K is much smaller (6.49 μ_B) than the corresponding values measured for $Gd_2Co_{12}As_7$ at the same temperatures. This difference can be attributed to the increase in the fraction of nonmagnetic Eu^{3+} ions as the temperature decreases. At 100 K, the average oxidation state of $\sim$+2.7 gives the expectation moment of 2.1 μ_B per Eu center, although the moments are not fully saturated at that temperature. A significantly higher saturation magnetization could be expected at 1.8 K, but based on the trend in the XANES data (Fig. S4), the average oxidation state of Eu becomes much closer to +3 at low temperatures, thus diminishing the Eu contribution to the total magnetization value. Therefore, as the temperature is lowered, the magnetic behavior of $Eu_2Co_{12}As_7$ should resemble more closely the behavior of $Y_2Co_{12}As_7$ with diamagnetic Y^{3+} ions.

$R_2Co_{12}As_7$(R=Tb, Dy). Both $Tb_2Co_{12}As_7$ and $Dy_2Co_{12}As_7$ show very similar magnetic behavior, with FM ordering of Co moments at 131 and 128 K, respectively, followed by ordering of R moments at 84 and 69 K, respectively (Fig. 8). Interestingly, as the temperature is lowered, the FC magnetic susceptibility reaches the maximum, then decreases to a certain point, and then exhibits a slight upturn at lower temperature. Such behavior, along with the divergence of the ZFC and FC susceptibility curves, can be attributed to the magnetocrystalline anisotropy of the rare-earth ions. The isothermal magnetization curves exhibit much faster initial rise at lower temperatures, which is also in agreement with the ordering of 4*f* moments. The M_{sat} values reached at 1.8 K and 7 T are 18.50 μ_B for $Tb_2Co_{12}As_7$ and 18.16 μ_B for $Dy_2Co_{12}As_7$, which is close to the theoretically expected contributions of 18 μ_B and 20 μ_B from two Tb^{3+} or two Dy^{3+} ions, respectively. Thus, it is difficult to conclusively establish the type of 4*f*-3*d* coupling in these materials. Given the more complex behavior of temperature-dependent magnetization at lower temperatures, further measurements, such as neutron scattering or X-ray magnetic circular dichroism spectroscopy experiments, are required to elucidate the magnetically ordered states of $Tb_2Co_{12}As_7$ and $Dy_2Co_{12}As_7$. Nevertheless, given the well-known trend for the reversal of the sign of 4*f*-3*d* magnetic exchange at the middle of lanthanide series (for the half-filled *f*-shell), we hypothesize that the 4*f*-3*d* coupling in these materials should be FM in nature. This assumption is further supported by properties of the later members of $R_2Co_{12}As_7$ series. It is also in agreement with our findings of AFM 4*f*-3*d* coupling in RCo_2P_2 and RCo_2As_2 structures with early lanthanides [25,26,33].

$R_2Co_{12}As_7$ (R=Ho, Er, Tm). As expected, these three compounds also exhibit FM ordering of Co moments at T_C equal to 139, 116, and 136 K, respectively (Figs. 9a and S8). The increase in the FC magnetic susceptibility at lower temperatures suggests the FM ordering of rare-earth moments, although the transition temperature is less clearly defined. The ordering is likely gradual, as also seen for the earlier compounds in the $R_2Co_{12}As_7$ series. The field-dependent magnetization measured at 100 K shows an initial rise of $\sim$2–3 μ_B (Fig. 9b), which is similar to the value observed for $Y_2Co_{12}As_7$. The magnetization curves recorded at 1.8 K exhibit much faster increase at low fields as compared to the magnetization measured at 100 K. Furthermore, the M_{sat} values observed at 1.8 K and 7 T are 21.6 μ_B for $Ho_2Co_{12}As_7$, 19.1 μ_B for $Er_2Co_{12}As_7$, and 14.6 μ_B for $Tm_2Co_{12}As_7$, which exceed the contributions of 20, 18, and 14, respectively, expected for the corresponding R^{3+} ions. Such observations support the FM coupling between the 4*f* and 3*d* moments in these materials.

Please cite this article as: X. Tan, et al., J. Solid State Chem. (2015), http://dx.doi.org/10.1016/j.jssc.2015.08.038

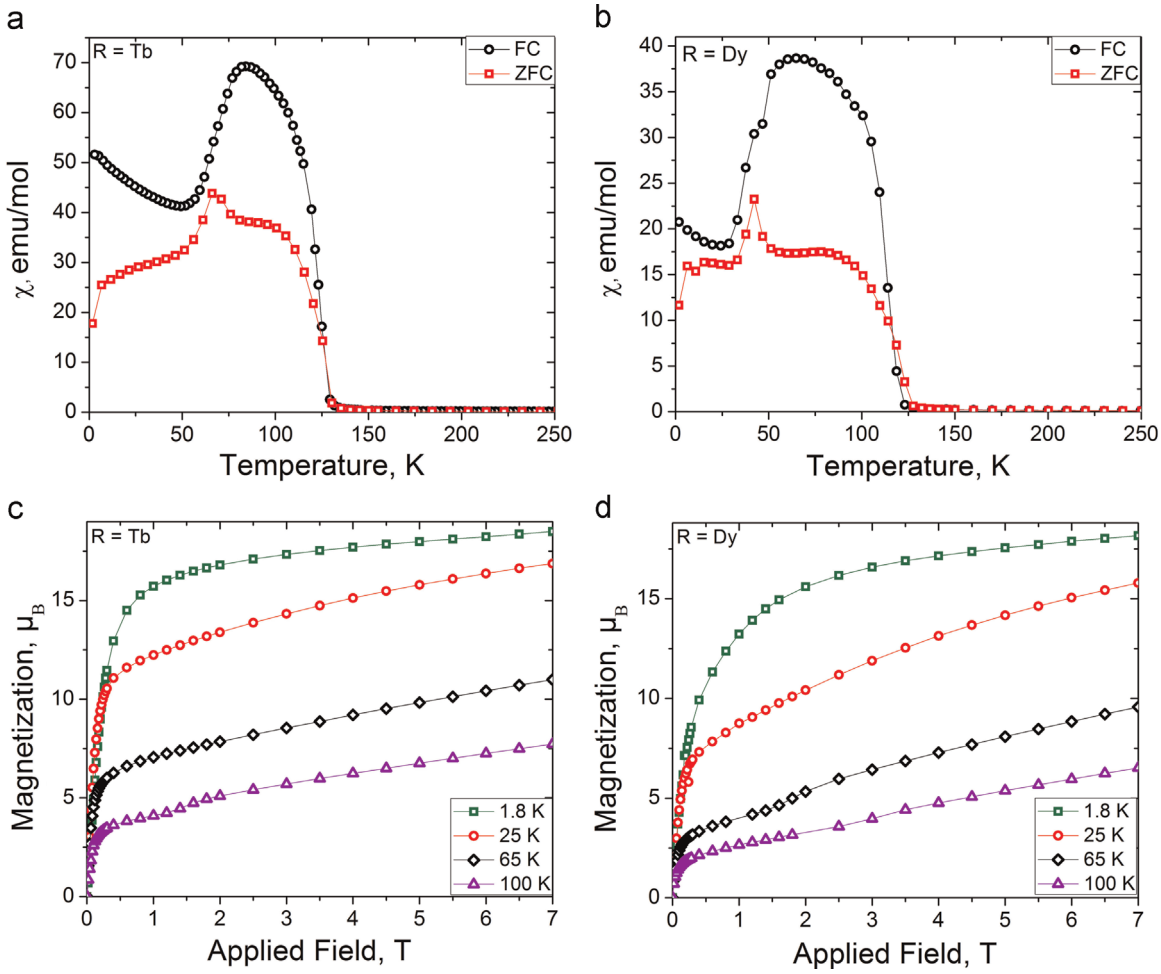

Fig. 8. Temperature dependence of zero-field-cooled (ZFC) and field-cooled (FC) magnetization measured at 1 mT for $Tb_2Co_{12}As_7$ (a) and $Dy_2Co_{12}As_7$ (b), and isothermal field dependence of magnetization measured at 1.8, 25, 65, and 100 K for $Tb_2Co_{12}As_7$ (c) and $Dy_2Co_{12}As_7$ (d).

3.4. *Neutron scattering*

To establish the structure of magnetically ordered states, neutron scattering experiments were performed on powder samples of $Nd_2Co_{12}As_7$ and $Ce_2Co_{12}As_7$.

$Nd_2Co_{12}As_7$. Initially, this material was examined by non-polarized neutron powder diffraction (NPD). Since no magnetic ordering is expected at 150 K, the NPD pattern collected at that temperature should be representative of the nuclear structure. The unit cell parameters refined from the NPD data were in good agreement with those obtained from the PXRD data (Table 4). The Rietveld refinement was performed using the structural model established from the single-crystal X-ray experiment and adding Bi as the second phase. Satisfactory convergence was achieved, indicating the molar fraction of Bi impurity as 5%.

Nuclear peaks (100) and (110), which were very weak at 150 K, increased in intensity slightly at 50 K and dramatically at 2 K (Fig. 10a). The pattern obtained at 50 K was refined similar to the one at 150 K, but with the addition of a magnetic phase located at the same atomic positions as the main nuclear phase, $Nd_2Co_{12}As_7$. Based on the magnetic measurements, we assumed only Co moments to be ordered at 50 K. The refinement resulted in magnetic moments of 0.2(1) μ_B on Co1 atom and 0.53(9) μ_B on Co2/Co3 atoms. The total magnetic moment is $0.2 \times 6 + 0.53 \times 6 = 4.3$ μ_B per f.u., which is close to the value of 3.9 μ_B obtained from magnetization data at 50 K.

The Rietveld refinement of NPD pattern obtained at 2 K was carried out assuming magnetic ordering in both Nd and Co sublattices. The magnetic phase was located at the atomic positions of the main nuclear phase. A satisfactory refinement was achieved only when Nd and Co moments were oriented antiparallel to each other, resulting in the FiM ground state (Fig. 10b). Attempts to model the magnetic structure with Nd and Co moments coupled FM to each other led to significantly larger refinement residuals (Fig. S9). The magnetic moments derived from the refinement were 1.6(2) μ_B for Nd, 0.22(7) μ_B for Co1, and 0.53(5) μ_B for Co2/Co3.

Polarized neutron scattering measurements were performed on the $Nd_2Co_{12}As_7$ sample placed in a vertical magnetic field of 0.1 T. The measurements were performed at 150, 50, and 5 K, for the spin of the incident neutron beam aligned parallel and antiparallel to the magnetic field direction. The experimental data and the calculated profiles are displayed in Fig. 11a. At 150 K, no magnetic signal was observed, as expected for a paramagnetic state. The spectrum obtained at 50 K confirmed the FM ordering of Co moments, with the calculated moment at Co1 site approximately three times smaller than the moment at Co2/Co3 site, in good agreement with the results of non-polarized NPD experiments. The spectrum was satisfactorily simulated with μ(Co1) = 0.1(1) μ_B and μ(Co2/Co3) = 0.3(1) μ_B. At 5 K, a strong scattering component emerged in the opposite direction, suggesting the ordering of Nd moments in the direction antiparallel to the Co moments. The data were modeled with μ (Nd) = −1.6 μ_B, μ(Co1) = 0.2(1) μ_B, and μ(Co2/Co3) = 0.6(1) μ_B, which agree very well with values obtained from the Rietveld refinement of the non-polarized NPD pattern recorded at 2 K. We would like to point

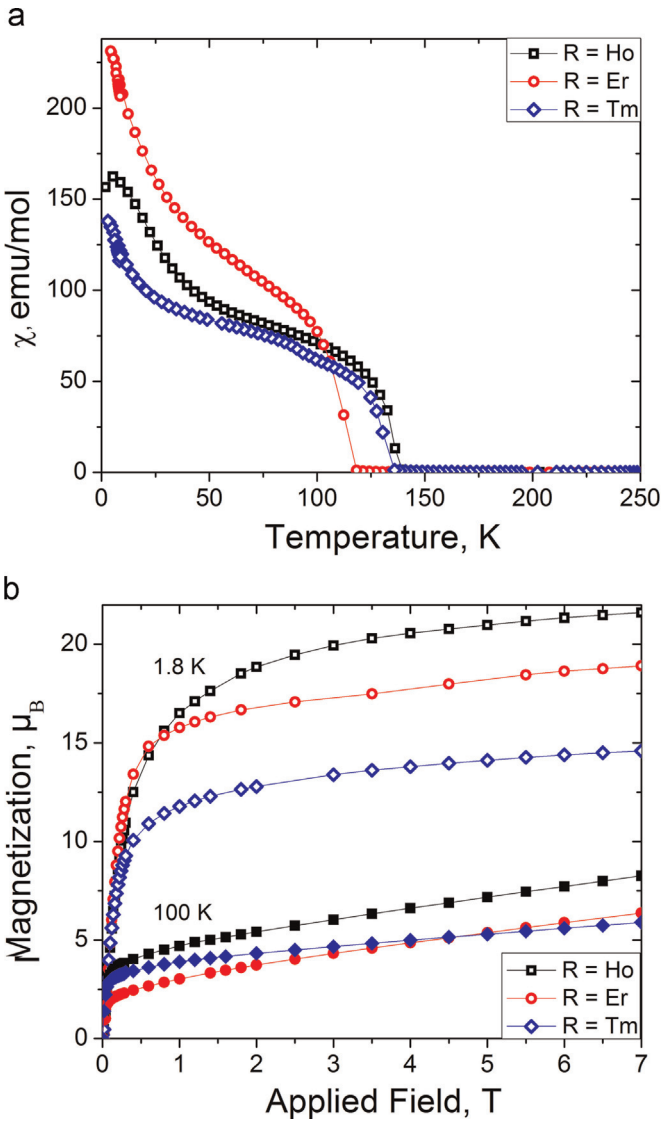

Fig. 9. (a) Temperature dependence of field-cooled magnetization at 1 mT and (b) isothermal field dependence of magnetization at 1.8 K (empty symbols) and 100 K (solid symbols) for $R_2Co_{12}As_7$ (R=Ho, Er, Tm).

Table 4
Unit cell parameters of $Nd_2Co_{12}As_7$ refined from neutron and X-ray powder diffraction data.

Compound	Method	*T*, K	*a*, Å	*c*, Å
$Nd_2Co_{12}As_7$	X-ray	298	9.443(4)	3.7896(8)
	neutron	150	9.4243(2)	3.7781(1)
	neutron	50	9.4201(1)	3.7733(1)
	neutron	2	9.4199(2)	3.7726(1)

out that setting the moments at all Co sites equal did not provide a satisfactory fit to either non-polarized or polarized neutron scattering data. A similar effect was observed by Jeitschko et al. in the analysis of neutron diffraction patterns of $R_2Co_{12}P_7$ (R=Pr, Nd, Ho), and the difference in the magnetic moment of crystallographically distinct Co centers was explained by their different coordination environments [19].

$Ce_2Co_{12}As_7$. Since the magnetic data suggested two successive FM phase transitions in $Ce_2Co_{12}As_7$, with rather weak saturation moments, non-polarized NPD data were not acquired because they would not have been sensitive enough to the magnetic order in this material. Initial polarized measurements were performed under the same conditions as in the case of $Nd_2Co_{12}As_7$, in vertical magnetic field of 0.1 T. Measurements at 150 and 50 K did not detect any magnetic signal. At 5 K, magnetic peaks were observed in the difference scattering (I^+–I^-). Surprisingly, the pattern observed suggests that the ordered Ce moment is very small, ~0.1(1) μ_B, and aligned parallel to the Co moments. Similar to the Nd-containing compound, the moment on the Co1 site (0.2 μ_B) was refined to be approximately three times smaller than that on the Co2/Co3 site (0.6 μ_B).

$Ce_2Co_{12}As_7$ was also examined by polarized neutron scattering under magnetic field of 2 T. The data were collected at 150, 50, and 1.5 K. Similar to the data obtained under 0.1 T, no magnetic signal was observed at 150 K. The spectra recorded at 50 K and 1.5 K were satisfactorily simulated with magnetic moments (in μ_B) on Ce, Co1, and Co2/Co3 sites equal to 0, 0.1(1), 0.2(1) and 0.1(1), 0.2(1), 0.6(1), respectively (Fig. 11b).

4. Conclusions

This work demonstrates that Bi flux can be used as effective reaction medium for the synthesis of ternary arsenides, $R_2Co_{12}As_7$ (R=Y, Ce–Yb). The reactions are usually complete within 7–10 days, and in the majority of cases single-phase products can be obtained. All $R_2Co_{12}As_7$ compounds crystallize in the $P6_3/m$ variant of the $Zr_2Fe_{12}P_7$ structure type. The higher symmetry results from the separation of the structure into domains characterized by the short-range $P\bar{6}$ symmetry. The study of the materials with transmission electron microscopy supported the structural model established from the single-crystal X-ray diffraction data.

The successful synthesis of phase-pure $R_2Co_{12}As_7$ materials allowed investigation of their magnetic properties. In general, the Co sublattice exhibits ferromagnetic ordering at 100–140 K, similar to the behavior of $R_2Co_{12}P_7$, in which the Co moments exhibit ferromagnetic ordering at 140–160 K. The lower-temperature magnetic behavior depends on the identity of lanthanide element. The 3*d*-4*f* exchange coupling is antiferromagnetic for R=Pr–Sm, but changes to ferromagnetic for R=Eu–Tm. This finding also agrees with the results of earlier determination of magnetic structures of $R_2Co_{12}P_7$ (R=Pr, Nd, Ho) by neutron diffraction, which revealed antiferromagnetic Pr–Co and Nd–Co coupling and ferromagnetic Ho–Co coupling [19]. Thus, we observe the change in the character of 3*d*-4*f* magnetic exchange at half-filling of the 4*f* shell. This is similar to observations made in other series of 3*d*-4*f* intermetallics [46–48], although the sign of exchange (ferro- or antiferromagnetic) can differ depending on the particular structure of a series [25].

Compounds with Ce, Eu, and Yb stand out from the general trend in the magnetic properties of $R_2Co_{12}As_7$, due to the mixed valence of these metals, which at 294 K exhibit the average oxidation states of +3.20, +2.47, and +2.91, respectively, as established by XANES spectroscopy. The deviation in magnetic properties is rather minor in the case of $Eu_2Co_{12}As_7$, which only exhibits somewhat higher ordering temperature than its Sm- and Gd-containing neighbors. $Ce_2Co_{12}As_7$, however, shows ferromagnetic 3*d*-4*f* exchange, which contrasts with ferrimagnetism established for the other $R_2Co_{12}As_7$ materials with the less than half-filled 4*f* shell. The ferromagnetic exchange in $Ce_2Co_{12}As_7$ and antiferromagnetic one in $Nd_2Co_{12}As_7$ were also confirmed by polarized neutron scattering experiments. Finally, in the case of $Yb_2Co_{12}As_7$, we could not find a clear signature of Yb contribution to the magnetic ordering. This effect might stem from delocalization of the Yb electron density through the 3*d*-5*d* hybridization, although further studies are required to understand the observed behavior.

Please cite this article as: X. Tan, et al., J. Solid State Chem. (2015), http://dx.doi.org/10.1016/j.jssc.2015.08.038

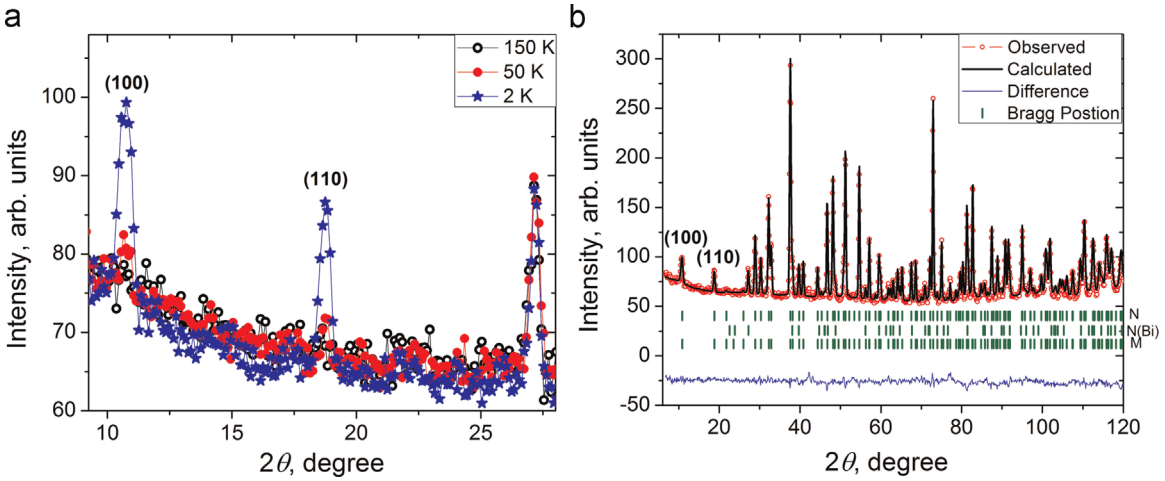

Fig. 10. (a) Fragments of neutron powder diffraction patterns of $Nd_2Co_{12}As_7$ emphasizing the growth of the (100) and (110) diffraction peaks with decreasing temperature. (b) Rietveld refinement of the neutron powder diffraction pattern of $Nd_2Co_{12}As_7$ collected at 2 K and 0 T, assuming antiferromagnetic 3*d*-4*f* coupling.

It should be pointed out that the number of known ternary structures in the R–Co–As systems is much smaller than the number of known R–Co–P materials. Therefore, we believe the use of Bi flux will afford the synthesis of other rare-earth cobalt arsenides and the growth of single crystals of these materials, hence detailed investigation of their physical properties. Efforts in this

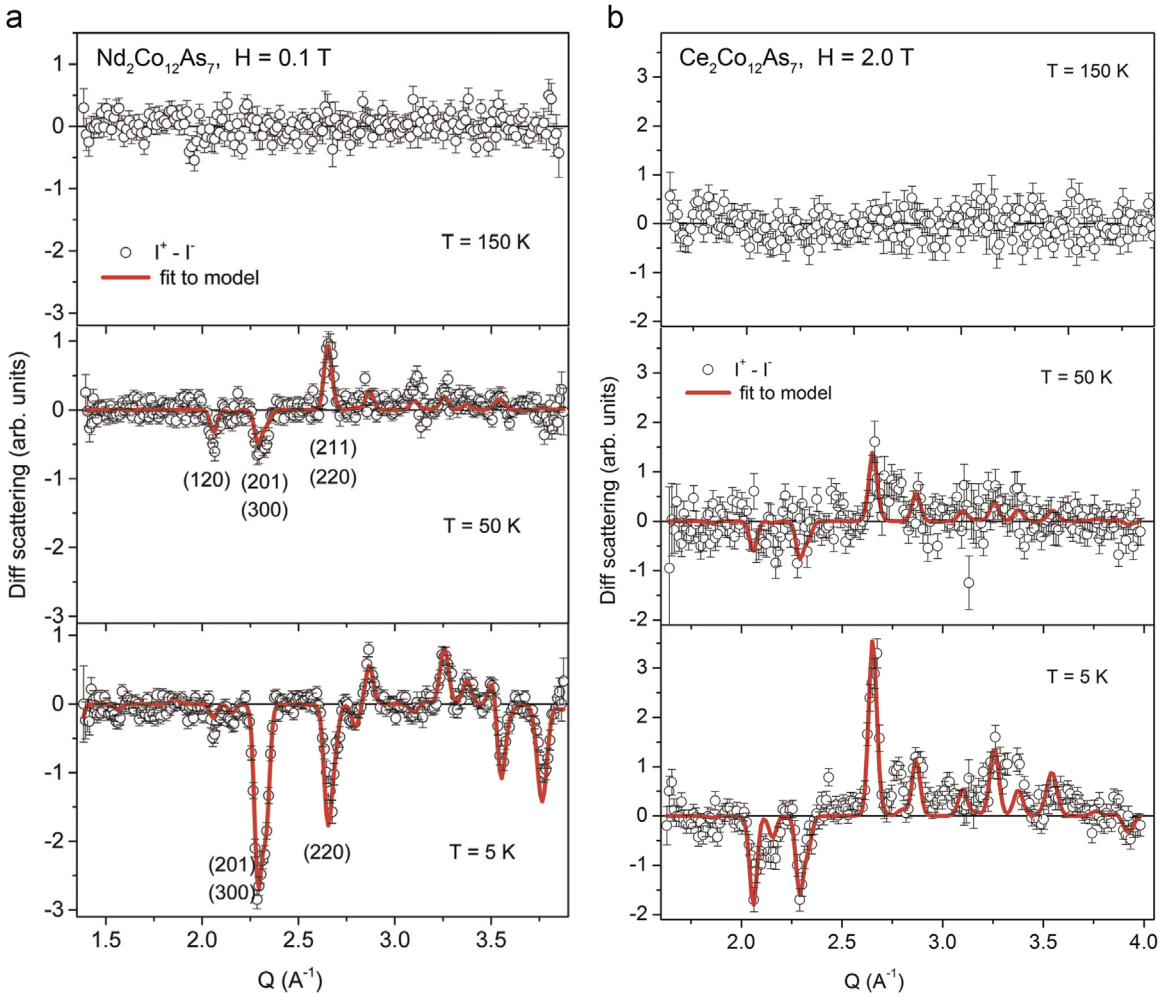

Fig. 11. Difference plots (I_+–I_-) of polarized neutron scattering profiles for (a) $Nd_2Co_{12}As_7$ at 0.1 T and 150, 50, and 5 K and (b) $Ce_2Co_{12}As_7$ at 2.0 T and 150, 50, and 1.5 K. The spin polarization of the incident neutron beam was aligned parallel (I_+) and antiparallel (I_-) to the magnetic field direction. The red lines show calculated profiles assuming the models discussed in the text. (For interpretation of the references to color in this figure legend, the reader is referred to the web version of this article.)

Please cite this article as: X. Tan, et al., J. Solid State Chem. (2015), http://dx.doi.org/10.1016/j.jssc.2015.08.038

direction are currently under way in our laboratories.

Acknowledgments

This work was supported by the National Science Foundation award DMR-1507233 to M.S. The work at the Oak Ridge National Laboratory was sponsored by the Scientific User Facilities Division, Office of Basic Energy Sciences, U.S. Department of Energy (DOE). V.O.G. thanks the help provided by the HYSPEC instrument team, B. Winn and M. Graves-Brook, during the polarized neutron scattering study. The TEM work was carried out at the electron microscopy facility at FSU which is funded and supported by the FSU Research Foundation, National High Magnetic Field Laboratory (NSF-DMR-0654118), and the State of Florida. The authors acknowledge Helmholtz-Zentrum Berlin and MAX IV Laboratory for providing the time at mySpot and I811 beamlines and Dr. Ivo Zizak (HZB), Dr. S. Carlson and Dr. K. Sigfridsson (MAX IV) for support during the experiment. A.P.M. and A.A.Y. thank the Russian Science Foundation (Project 14-22-00098) for support.

Appendix A. Supplementary Information

Supplementary data associated with this article can be found in the online version at http://dx.doi.org/10.1016/j.jssc.2015.08.038.

References

[1] O. Gutfleisch, M.A. Willard, E. Brück, C.H. Chen, S.G. Sankar, J.P. Liu, Adv. Mater. 23 (2011) 821–842.
[2] A.E. Clark, Magnetostrictive rare earth-Fe_2 compounds, in: E.P. Wolfarth (Ed.), Handbook of Ferromagnetic Materials, North-Holland, Amsterdam, 1980, pp. 531–589.
[3] A.E. Clark, M. Wun-Fogle, Proc. SPIE 4699 (2002) 421–436.
[4] V. Franco, J.S. Blazquez, B. Ingale, A. Conde, Annu. Rev. Mater. Res. 42 (2012) 305–342.
[5] K.H.J. Buschow, Rep. Prog. Phys. 40 (1977) 1179–1256.
[6] A.A. Gomes, A.P. Guimaraes, J. Phys. F 4 (1974) 1454–1465.
[7] Z.D. Zhang, Handb. Adv. Magn. Mater. 4 (2006) 50–85.
[8] K. Kovnir, M. Shatruk, Eur. J. Inorg. Chem. (2011) 3955–3962 2011.
[9] M.G. Kanatzidis, R. Pottgen, W. Jeitschko, Angew. Chem. Int. Ed. 44 (2005) 6996–7023.
[10] P. Villars, L.D. Calvert, Pearson's Handbook of Crystallographic Data for Intermetallic Phases, ASM International, Materials Park, OH, 1991.
[11] E. Mörsen, B.D. Mosel, W. Müller-Warmuth, M. Reehuis, W. Jeitschko, J. Phys. Chem. Solids 49 (1988) 785–795.
[12] M. Reehuis, W. Jeitschko, E. Mörsen, W. Müller-Warmuth, J. Less-Common, Metals 139 (1988) 359–369.
[13] M. Reehuis, W. Jeitschko, J. Phys. Chem. Solids 50 (1989) 563–569.
[14] M. Reehuis, W. Jeitschko, J. Phys. Chem. Solids 51 (1990) 961–968.
[15] M. Reehuis, W. Jeitschko, M.H. Möller, P.J. Brown, J. Phys. Chem. Solids 53 (1992) 687–690.
[16] H. Raffius, E. Mörsen, B.D. Mosel, W. Müller-Warmuth, W. Jeitschko, L. Terbüchte, T. Vomhof, J. Phys. Chem. Solids 54 (1993) 135–144.
[17] M. Reehuis, P.J. Brown, W. Jeitschko, M.H. Möller, T. Vomhof, J. Phys. Chem. Solids 54 (1993) 469–475.
[18] M. Reehuis, C. Ritter, R. Ballou, W. Jeitschko, J. Magn. Magn. Mater. 138 (1994) 85–93.
[19] M. Reehuis, B. Ouladdiaf, W. Jeitschko, T. Vomhof, B. Zimmer, E. Ressouche, J. Alloy. Compd. 261 (1997) 1–11.
[20] M. Chefki, M.M. Abd-Elmeguid, H. Micklitz, C. Huhnt, W. Schlabitz, M. Reehuis, W. Jeitschko, Phys. Rev. Lett. 80 (1998) 802–805.
[21] M. Reehuis, W. Jeitschko, G. Kotzyba, B. Zimmer, X. Hu, J. Alloy. Compd. 266 (1998) 54–60.
[22] K. Kovnir, C.M. Thompson, H.D. Zhou, C.R. Wiebe, M. Shatruk, Chem. Mater. 22 (2010) 1704–1713.
[23] K. Kovnir, W.M. Reiff, A.P. Menushenkov, A.A. Yaroslavtsev, R.V. Chernikov, M. Shatruk, Chem. Mater. 23 (2011) 3021–3024.
[24] K. Kovnir, V.O. Garlea, C.M. Thompson, H.D. Zhou, W.M. Reiff, A. Ozarowski, M. Shatruk, Inorg. Chem. 50 (2011) 10274–10283.
[25] K. Kovnir, C.M. Thompson, V.O. Garlea, D. Haskel, A.A. Polyanskii, H.D. Zhou, M. Shatruk, Phys. Rev. B 88 (2013) 104429.
[26] C.M. Thompson, K. Kovnir, V.O. Garlea, E.S. Choi, H.D. Zhou, M. Shatruk, J. Mater. Chem. C 2 (2014) 7561–7569.
[27] C.M. Thompson, K. Kovnir, H. Zhou, M. Shatruk, Z. Anorg. Allg. Chem. 637 (2011) 2013–2017.
[28] R. Marchand, W. Jeitschko, J. Solid State Chem. 24 (1978) 351–357.
[29] S. Oryshchyn, S. Stoyko, O. Zhak, Visnyk Lviv. Univ. Ser. Chem. 53 (2012) 146–150.
[30] S. Stoyko, S. Oryshchyn, Visnyk Lviv. Univ. Ser. Chem. (2010) 74–78.
[31] J. Ballinger, L.E. Wenger, Y.K. Vohra, A.S. Sefat, J. Appl. Phys. 111 (2012).
[32] C.M. Thompson, K. Kovnir, S. Eveland, M.J. Herring, M. Shatruk, Chem. Commun. 47 (2011) 5563–5565.
[33] C.M. Thompson, X.Y. Tan, K. Kovnir, V.O. Garlea, A.A. Gippius, A.A. Yaroslavtsev, A.P. Menushenkov, R.V. Chernikov, N. Büttgen, W. Krätschmer, Y. V. Zubavichus, M. Shatruk, Chem. Mater. 26 (2014) 3825–3837.
[34] HighScore Plus, PANalytical B.V., Almelo, Netherlands, 2006.
[35] SMART and SAINT, Bruker AXS Inc., Madison, WI, USA, 2007.
[36] G.M. Sheldrick, Acta Crystallogr. Sect. A A64 (2008) 112–122.
[37] V.O. Garlea, B.C. Chakoumakos, S.A. Moore, G.B. Taylor, T. Chae, R.G. Maples, R. A. Riedel, G.W. Lynn, D.L. Selby, Appl. Phys. A 99 (2010) 531–535.
[38] J. Rodríguez-Carvajal, Physica B 192 (1993) 55–69.
[39] B. Winn, U. Filges, V.O. Garlea, M. Graves-Brook, M. Hagen, C.Y. Jiang, M. Kenzelmann, L. Passell, S.M. Shapiro, X. Tong, I. Zaliznyak, EPJ Web Conf. 83 (2015) 03017.
[40] A.S. Wills, E. Lelièvre-Berna, F. Tasset, J. Schweizer, R. Ballou, Physica B 356 (2005) 254–258.
[41] E. Lelièvre-Berna, A.S. Wills, E. Bourgeat-Lami, A. Dee, T. Hansen, P.F. Henry, A. Poole, M. Thomas, X. Tonon, J. Torregrossa, K.H. Andersen, F. Bordenave, D. Jullien, P. Mouveau, B. Guerard, G. Manzin, Meas. Sci. Technol. 21 (2010).
[42] W. Jeitschko, D.J. Braun, R.H. Ashcraft, R. Marchand, J. Solid State Chem. 25 (1978) 309–313.
[43] A. Hellmann, A. Mewis, Z. Anorg. Allg. Chem. 627 (2001) 1357–1364.
[44] W. Jeitschko, U. Meisen, J. Albering, Dalton Trans. 39 (2010) 6067–6073.
[45] W. Jeitschko, U. Meisen, E.J. Reinbold, Z. Anorg. Allg. Chem. 638 (2012) 770–778.
[46] K.H.J. Buschow, F.R. de Boer, Physics of Magnetism and Magnetic Materials, Kluwer Academic, New York, 2004.
[47] M.S.S. Brooks, B. Johansson, Handb. Magn. Mater. 7 (1993) 139–230.
[48] N.H. Duc, P.E. Brommer, Handb. Magn. Mater. 12 (1999) 259–394.